DRUG MONITORING

Resilient nanostructured bioanalytic microneedle longitudinally monitors preclinical renal and hepatic drug clearance and dysfunction

**Jialun Zhu[1], Xuanbing Cheng[1], Mohammadreza Bahramian[1,2], Kuanming Yao[1], Zongqi Li[1,3], Bintao Hu[3], Tsung-Yu Wu[1], Kiarash A. Sabet[1], Jiarui Cui[1], Jiawei Tan[1,3], Junjie Fang[1], Yifu Li[1], Connie Ho[1,2], Joshua Ng[1,3], Anthony Sung[1,4], Isabel Romero[5], Shuyu Lin[1], Yichao Zhao[1,6,7,8], Kaiji Zhang[1], Ryan Chaiyakul[1], Hanie Yousefi[9,10], Connor D. Flynn[10,11], Jagotamoy Das[11], David Jelinek[5], Laurent Voisin[5], Aaron Ambrus[5], Ao Zhang[3], Yitian Chi[2], Yu Chen[12], Chong Liu[12], Hilary A. Coller[5,13,14], Benjamin M. Wu[3,15,16,17], Nanthia Suthana[15,18,19,20], Shana O. Kelley[9,10,11,21,22,23,24], Carlos Milla[25], Ira Kurtz[26,27], Sam Emaminejad[1,15,16]*

Wearable microneedle biosensors promise real-time molecular monitoring for precision medicine but are limited by low sensitivity and tissue abrasion. Overcoming these challenges, we recast electrode functionality not merely as a sensing substrate but as a mechanism for resilient, high signal-to-noise ratio (SNR) measurements in tissue. Our microneedle-based resilient nanostructured bioelectrode (RNB) is fabricated using a bilayer process that strengthens the electrode with a micrometer-thick gold adhesion layer and reduces fabrication-induced stress through controlled dealloying. The resulting RNBs are corrosion resistant, stable over a wide potential window, and have an artifact-free, nanocavity-textured interface. They integrate receptor-based electrochemical biosensors with enhanced SNR through increased active area, diffusion, and antifouling while remaining abrasion immune in megapascal-stiff tissues. The RNB extended in vivo biosensor lifetime for pharmacokinetics monitoring to 6 days in a freely moving rat. Paired with a blood–interstitial fluid equilibrium–based bioanalytical framework, the RNB accurately derived blood-equivalent pharmacokinetic parameters, enabling not only precision dosing of narrow therapeutic index drugs but also the direct assessment of hepatic and renal clearance. In hepatic studies, the RNB revealed delayed clearance of a chemotherapeutic (irinotecan) in liver-damaged models. In renal studies, RNB recordings correlated with blood antibiotic pharmacokinetics across chronic kidney disease severities. The RNB detected renal impairment earlier than conventional biomarker thresholds through drug clearance quantification and captured recovery under therapeutic intervention. These results establish the RNB as a viable microneedle platform for high-fidelity in vivo deployment of electrochemical biosensors, enabling minimally invasive, longitudinal monitoring of low-concentration analytes and real-time assessment of organ function.

INTRODUCTION

Tailoring treatment strategies to an individual's dynamic biochemistry and the physiological and metabolic responses of organs like the kidney and liver is the cornerstone of personalized and precision medicine (*1*). This approach is essential for mitigating life-threatening complications associated with dosing of drugs with narrow therapeutic indices (NTIs) (*2*, *3*), where underdosing reduces efficacy and overdosing causes toxicity and organ dysfunction (*4*, *5*). Current clinical dosing practices rely on nonspecific patient characteristics (age, height, and weight) and sporadic blood tests, which only provide delayed snapshots of drug concentration and organ function. Statistical models that aim to relate static blood measurements to dynamic drug clearance and organ function often face challenges in accounting for individual lifestyle, demographic, and

[1]Interconnected and Integrated Bioelectronics Lab (I²BL), Department of Electrical and Computer Engineering, Samueli School of Engineering, University of California, Los Angeles, Los Angeles, CA 90095,USA. [2]Department of Mechanical and Aerospace Engineering, University of California, Los Angeles, Los Angeles, CA 90095, USA. [3]Department of Materials Science and Engineering, Samueli School of Engineering, University of California, Los Angeles, Los Angeles, CA 90095,USA. [4]Department of Chemical and Biomolecular Engineering, Samueli School of Engineering, University of California, Los Angeles, Los Angeles, CA 90095,USA. [5]Department of Molecular, Cell, and Developmental Biology, University of California, Los Angeles, Los Angeles, CA 90095,USA. [6]David H. Koch Institute for Integrative Cancer Research, Massachusetts Institute of Technology, Cambridge, MA 02139, USA. [7]Department of Anesthesiology, Critical Care Pain Medicine, Boston Children's Hospital, Boston, MA 02115, USA. [8]Department of Chemical Engineering, Massachusetts Institute of Technology, Cambridge, MA 02139, USA. [9]Department of Biomedical Engineering, McCormick School of Engineering, Northwestern University, Evanston, IL 60208, USA. [10]Chan Zuckerberg Biohub Chicago, Chicago, IL 60642, USA. [11]Department of Chemistry, Weinberg College of Arts and Sciences, Northwestern University, Evanston, IL 60208, USA. [12]Department of Chemistry and Biochemistry, University of California, Los Angeles, Los Angeles, CA 90095, USA. [13]Department of Biological Chemistry, David Geffen School of Medicine, University of California, Los Angeles, Los Angeles, CA 90095, USA. [14]Molecular Biology Institute, University of California, Los Angeles, Los Angeles, CA 90095, USA. [15]Department of Bioengineering, University of California, Los Angeles, Los Angeles, CA 90095, USA. [16]California NanoSystems Institute (CNSI), University of California, Los Angeles, Los Angeles, CA 90095, USA. [17]ADA Forsyth Institute, Somerville, MA 02143, USA. [18]Department of Psychology, University of California, Los Angeles, Los Angeles, CA 90095, USA. [19]Department of Neurosurgery, Duke University, Durham, NC 27710, USA. [20]Department of Biomedical Engineering, Duke University, Durham, NC 27708, USA. [21]Robert H. Lurie Comprehensive Cancer Center, Northwestern University, Chicago, IL 60611, USA. [22]Department of Biochemistry, Feinberg School of Medicine, Northwestern University, Chicago, IL 60611, USA. [23]International Institute for Nanotechnology, Northwestern University, Evanston, IL 60208, USA. [24]Simpson Querrey Institute, Northwestern University, Chicago, IL 60611, USA. [25]Stanford Cystic Fibrosis Center, Center for Excellence in Pulmonary Biology, Stanford School of Medicine, Stanford, CA 94305, USA. [26]Department of Medicine, David Geffen School of Medicine, University of California, Los Angeles, Los Angeles, CA 90095, USA. [27]Brain Research Institute, David Geffen School of Medicine, University of California, Los Angeles, Los Angeles, CA 90095, USA.
*Corresponding author. Email: emaminejad@ucla.edu

genetic variations (*6*), leading to poor outcomes for underrepresented populations (*7*). Moreover, surrogate biomarkers used to assess clearance and organ function, such as creatinine for kidney health, do not account for drug-specific metabolic patterns, limiting their predictive value in tailoring personalized therapeutic interventions (*8*).

Wearable microneedle sensors offer a viable solution to these limitations by enabling monitoring of molecular processes in the interstitial fluid (ISF) of skin tissue (*9*). Nonetheless, microneedle sensors with established clinical utility are largely limited to enzymatic detection of abundant metabolites, such as glucose, using oxidase-based electrochemical conversion, which is not directly applicable to therapeutic drug monitoring (TDM) (*10*). Incorporating monolayer electrochemistry, such as redox reporter–coupled aptamers, provides a promising path toward real-time, continuous monitoring of low-concentration analytes, including pharmaceuticals that lack enzymatic-detection pathways (*11*). These sensing interfaces have shown promise for TDM in surgically implanted probes deployed in veins (*12*). However, adapting them for the envisioned minimally invasive applications, requiring robust integration into self-deployable microneedles, remains constrained by challenges in device functionality and data interpretation related to in-tissue operation, which imposes additional complexities beyond those encountered in blood-based sensing (*13*).

From a device engineering perspective, miniaturizing microneedle tips, a necessity for minimal invasiveness, inevitably reduces signal intensity (*14*), with friction in deformable, viscoelastic tissue further challenging the biosensor's fidelity. Attempts to address these issues by decoupling microneedles from sensing electrodes (sampling-then-sensing) incur substantial analyte dilution and diffusion delays comparable to drug clearance timescales (for example, a 1-mm distance causes a 30-min delay for vancomycin) (*15*). Nanostructuring microneedle electrodes can enhance signal without such trade-offs (*16*); however, current implementations are vulnerable to device failures caused by mechanical stress during fabrication, insertion, or operation. For example, extruded interfaces like nanodendrite fractal structures, commonly adopted for their ease of fabrication, are prone to breakage at the stress-concentrated dendrite base. Meanwhile, embedded nanostructures with nanocavity features, which could offer added protection to the sensing layer (*17*–*19*), are susceptible to film cracking and decohesion caused by the large stress introduced when adapting conventional top-down fabrication methods to irregular microneedle surfaces (*20*). Consequently, the lack of suitable tools for high–temporal resolution ISF data acquisition has led to the absence of interpretability frameworks. This has left correlations between peripheral ISF and blood-based pharmacokinetic (PK) parameters largely phenomenological, with the link between ISF readings and metabolic organ clearance still unexplored (*16*, *21*, *22*).

Here, we overcome these limitations by recasting electrode functionality not merely as a substrate for the sensing interface but also as a mechanism to achieve resilience and enhance signal-to-noise ratio (SNR) in tissue. Accordingly, we developed a microneedle-based resilient nanostructured bioelectrode (RNB) hosting electrochemical monolayer receptor–based sensing interfaces for reliable in-tissue ISF analysis. Configured for prolonged therapeutic monitoring in the dermal space and paired with an ISF–blood diffusion–based bioanalytical framework, the RNB enables minimally invasive derivation of blood-equivalent PK parameters and assessment of preclinical renal and hepatic drug clearance.

RESULTS

Overview of RNB development and performance

To overcome limitations of traditional TDM, we designed the RNB microneedle platform that directly measures ISF pharmacokinetics and assesses renal and hepatic clearance (fig. S1, A and B). To ensure robust in-tissue operation, RNB features an embedded nanoporous interface, which helps to protect the sensing layer from tissue abrasion and support biosensing in stiff tissues. The nanostructured interface is expected to enhance signal quality by increasing electrochemically active surface area and facilitating mass transport in the porous network while limiting access of larger biofouling species through size-based exclusion (Fig. 1A). Our nanoporous interface fabrication strategy aims to simultaneously (i) enhance film stretch strength through the use of a micrometer-thick homogeneous gold adhesion layer and (ii) minimize fabrication stress by reducing the dealloying speed through a controlled electrochemical etching process during gold nanoporous layer formation (Fig. 1B and fig. S2). This approach provides a substantial margin for bridging the film strength–versus–fabrication stress gap encountered in traditional methods using Ti as an adhesion material (fig. S3, A to C).

Leveraging the RNB's high-SNR in vivo performance and built-in tissue-specific kinetic differential measurement (tKDM), we established a bioanalytical framework to quantify central-compartment PK parameters, including half-life, total drug exposure, and clearance for NTI therapeutics (Fig. 1C and fig. S4). These parameters provide the quantitative basis for personalized and precision medicine. Beyond aiding dosing adjustments, we demonstrated the platform's ability to provide early, actionable insights into organ dysfunction by capturing kinetic data on drug clearance by the liver or kidney (Fig. 1D). By elucidating the complex biochemical relationships between peripheral tissue dynamics and organ function, this platform enables patient-centric strategies in precision dosing and drug-specific organ health monitoring.

RNB fabrication and characterization

To fabricate the RNB, we first performed electrochemical plating of a micrometer-thick gold layer (thickness ~20 μm) onto a clinical-grade electrically conductive needle (Fig. 2, A and B), forming a chemically inert, homogeneous, and robust adhesion layer to support the nanostructured interfacial layer. The electrochemical plating promotes passive nucleation, improving gold coverage over the microneedle's native surface irregularities, such as steps or defects, effectively isolating the substrate from the electrolyte and suppressing undesirable reactions. The micrometer-thick adhesion layer enhanced its lateral stretch strength and protected electrodes from subsequent electrode modification steps such as dealloying, unlike traditional nanometer-thin layers that are prone to surface cracking (Fig. 1B and fig. S3) (*23*). In addition, electrochemical plating offered high material utilization, contributing to the device's low fabrication cost (table S1).

To assess electrochemical stability, we characterized the operating potential window of the RNB electrodes using cyclic voltammetry (CV) in phosphate-buffered saline (PBS) (*24*). The micrometer-thick homogeneous gold adhesion layer allowed the RNB to remain stable up to +1 V (versus Ag/AgCl), whereas conventional electrodes with

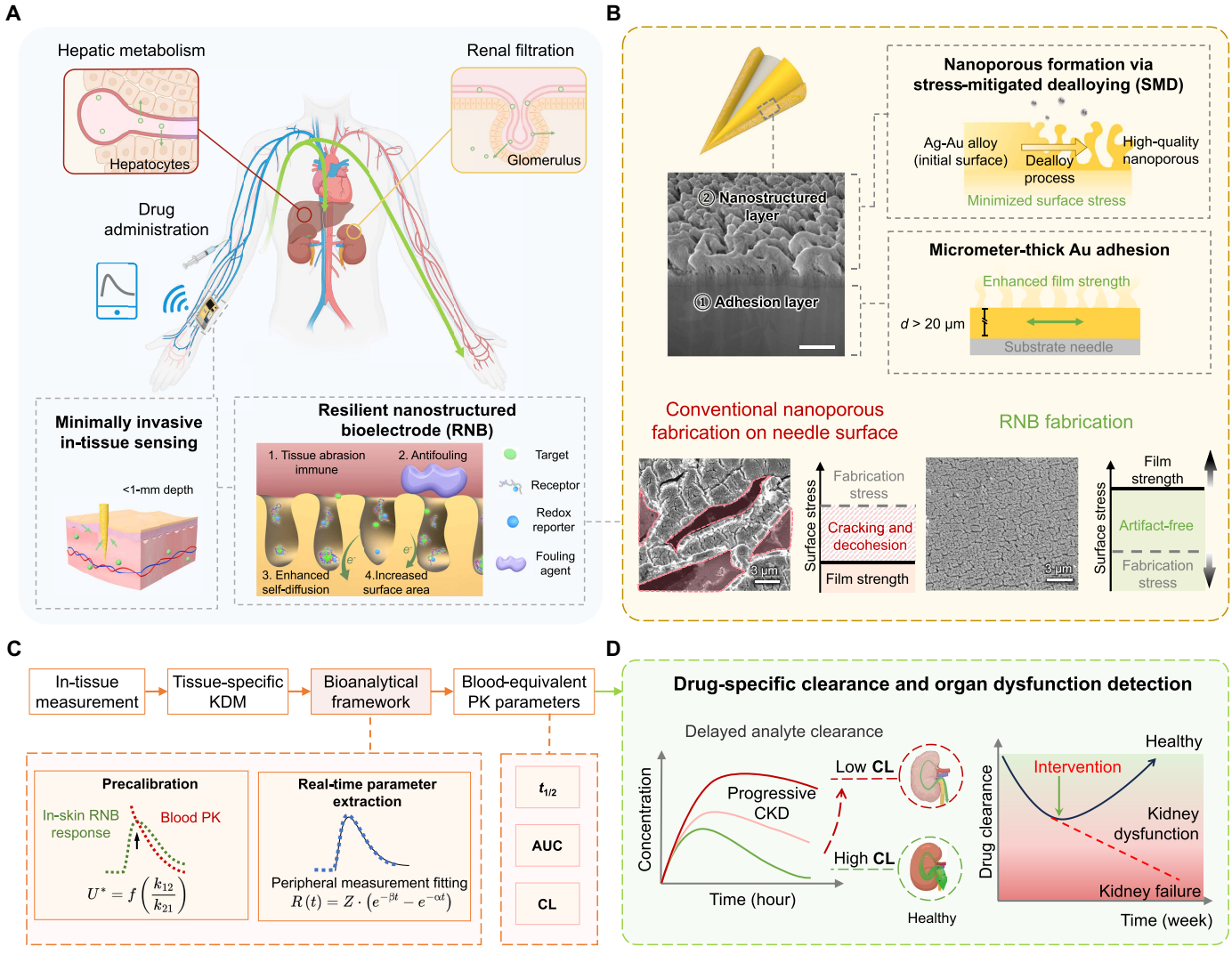

Fig. 1. Wearable therapeutic drug and metabolic function monitoring through RNB. (**A**) Schematic illustrating wearable monitoring of therapeutic drug and metabolic functions through minimally invasive in-tissue sensing by the RNB. Created in part with BioRender.com. (**B**) Bilayer structure of the RNB. Top left: SEM image of the cross section of the bilayer structure. Scale bar, 400 nm. Top right: The high-quality nanoporous layer fabricated from stress-mitigated dealloy with minimized surface stress; thick homogeneous gold adhesion layer ensures film strength and minimizes surface cracking. Bottom left: SEM image of a nanoporous structure fabricated using conventional methods, involving a thin Ti adhesion layer and rushed electrochemical etching. Bottom right: SEM image of a nanoporous structure fabricated using our method. The associated plots illustrate the relative relationship of film strength and fabrication-induced stress in both cases. (**C**) Bioanalytical framework for device calibration and inference of the blood-equivalent PK parameters including half-life ($t_{1/2}$), total drug exposure [area under the curve (AUC)], and drug clearance (CL). (**D**) Direct organ function assessment through real-time PK measurements. Left: Changes in pharmacokinetics, with reduced drug clearance indicating the onset of organ dysfunction. Right: Quantified PK parameters (drug clearance) facilitate early detection of organ dysfunction and enable timely intervention.

a sputtered heterogeneous Ti adhesion layer were limited to +0.3 V because of cracking and substrate exposure, as evidenced by the surge in current at higher-voltage conditions (fig. S5). The expanded potential window of the RNB supports a broader range of electrochemical detection modalities, as illustrated by the overlay of the redox potentials of common biosensing reporters (Fig. 2C) (*25*).

To assess electrodes' electrochemical durability and corrosion resistance, we subjected gold nanoporous electrodes to prolonged interrogation at +0.5 V (versus Ag/AgCl) in PBS, comparing three adhesion layer conditions: homogeneous gold adhesion (micrometer-thick gold used in RNB), conventional thin heterogeneous adhesion (50 nm sputtered), and bare nanoporous gold without an adhesion layer. Electrochemical surface area (ECSA) measurements were obtained through intermittent CV scans at varying rates (Fig. 2D) (*26*). Electrodes with heterogeneous adhesion exhibited larger corrosion currents because of undesirable reactions from the exposed underlying materials (fig. S6). These electrodes showed rapid ECSA increases, indicative of etching and delamination, leading to complete dissolution at about 30 min (Fig. 2E, top, and movie S1). In contrast, RNB electrodes demonstrated minimal ECSA changes, maintaining their structural integrity during 42 hours of continuous interrogation (Fig. 2, D and E, bottom), confirming their superior corrosion resistance.

To create an embedded gold nanostructure interface, we devised a top-down fabrication approach augmenting Au/Ag cosputtering

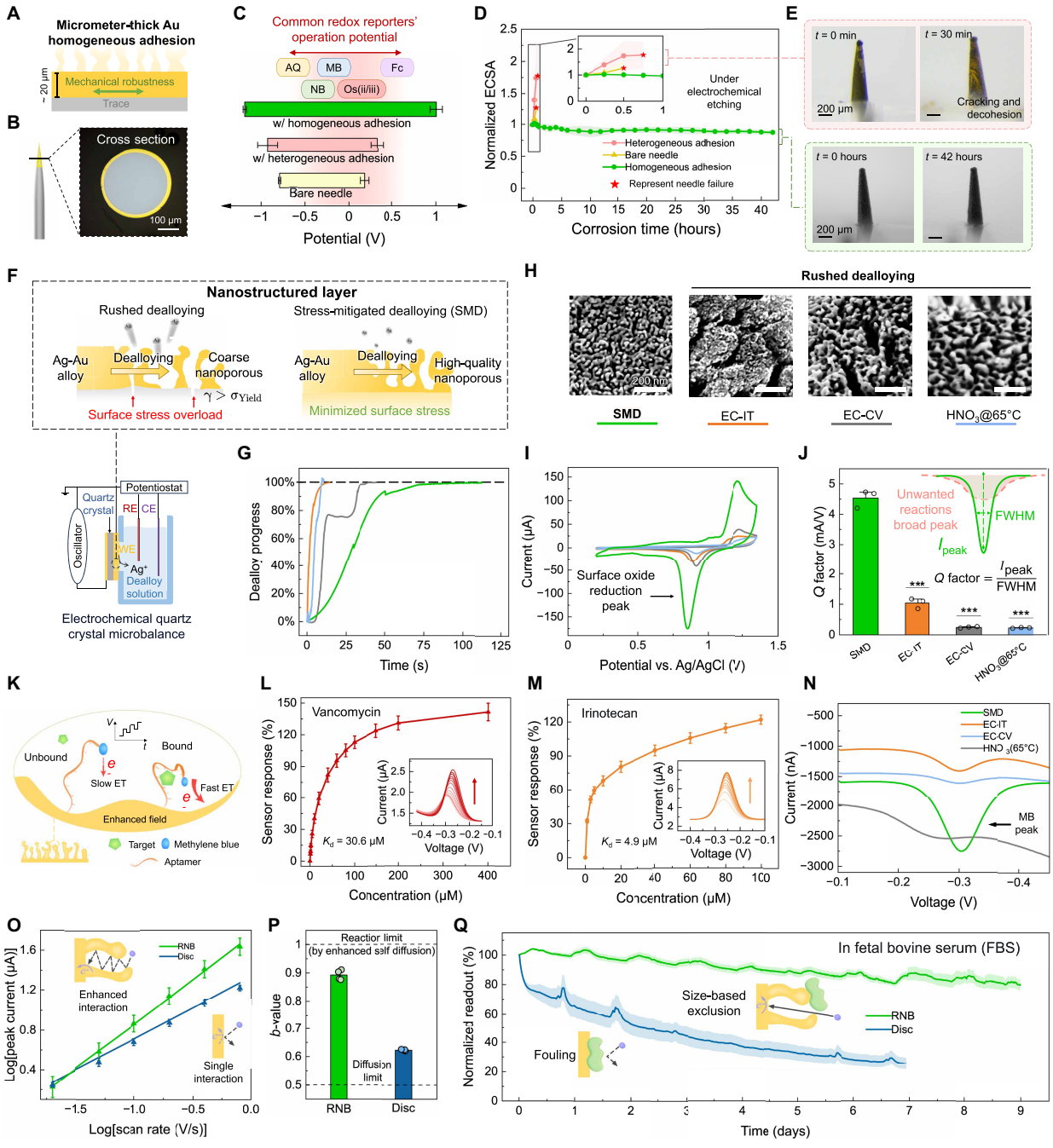

Fig. 2. Fabrication and functionalization of RNB for electrochemical sensors. (**A**) Schematic of the homogeneous gold adhesion layer. (**B**) Cross-sectional optical microscopy images of RNB, showing the gold adhesion layer (golden) and the metal needle substrate (silvery). (**C**) Potential window of nanoporous electrodes with various adhesion layers. Top symbols represent characteristic redox voltages for common redox reporters: AQ, anthraquinone; NB, Nile blue; MB, methylene blue; Os(ii/iii), Os(ii/iii) organometallic complex; Fc, ferrocene. (**D**) ECSA changes after interrogated at +0.5 V (versus Ag/AgCl) in PBS. (**E**) Microscopy images comparing postetching morphology between heterogeneous adhesion (top) and homogeneous adhesion (bottom). (**F**) Schematic of nanoporous structure formation by silver dealloying and dynamic monitoring by EQCM. Top left: Traditional rushed dealloying leads to surface cracking and decohesion; top right: SMD controls dealloying speed, minimizing surface stress; bottom: EQCM measurement of weight change during dealloying. RE, reference electrode; CE, counter electrode; WE, working electrode. (**G** to **J**) Dealloying profiles (G), SEM images (H), gold ORR CV curve (I), and quality factors from the ORR peak (J) for different dealloying methods: SMD, EC-IT (constant voltage), EC-CV, and HNO_3@65°C (immersing electrode in 70–wt % HNO_3 at 65°C). ***$P < 0.001$, two-tailed, two-sample t tests with the RNB group. (**K**) Sensing mechanism of MB-aptamer sensor. ET represents electron transfer. (**L** and **M**) Sensor response of vancomycin (L) and irinotecan (M) using RNB. Insets show raw SWV with arrows indicating increasing concentration. (**N**) Comparison of vancomycin sensor signal from electrodes fabricated by different dealloying methods (SWV at 60 Hz). (**O**) CV peak current of MB versus scan rate for RNB and disc electrodes. Inset illustrates enhanced multiple electrode-analyte interactions (top) for RNB and single interaction (bottom) for disc electrodes. (**P**) b-values derived from (O). (**Q**) SWV signal decay in fetal bovine serum for vancomycin sensors. The inset illustrates size-based protein blocking for RNB and fouling for disc electrodes. Shaded areas or error bars represent SD ($n = 3$).

with stress-mitigated dealloying (SMD). Traditional dealloying techniques rely on strong acid etching and lack precise control over reaction kinetics, making the resulting nanoporous structures susceptible to abrupt volume contraction, cracking, and decohesion (Fig. 2F, top left) (*27*, *28*). SMD overcomes these limitations by using a controlled electrochemical dealloying process with a slow voltage ramp-up rate of 5 mV/s. This approach allows gold atoms to diffuse and reorganize with low surface stress, forming a highly ordered nanoporous structure (Fig. 2F, top right) (*29*). The reduced dealloying rate was reflected in dealloy currents observed with various dealloying methods, including CV, constant voltage [denoted as current-time (*I*-*T*)], and nitric acid (HNO_3)–based methods (fig. S7). We further confirmed the SMD's reduced dealloying rate by recording and comparing electrode mass changes across different dealloy methods using an electrochemical quartz crystal microbalance (EQCM; Fig. 2F, bottom) (*30*). The SMD took more than 60 s to complete 95% of the dealloy process, whereas the other methods reach the same extent of dealloying in less than 33 s (Fig. 2G). Scanning electron microscopy (SEM) images revealed smoother ligaments and smaller feature sizes in nanoporous structures produced by SMD compared with rushed dealloying techniques (Fig. 2H).

To evaluate the quality of the resulting nanoporous electrodes, we analyzed the surface gold oxide reduction reaction (ORR) using CV in acid solution (Fig. 2I). The broadening of the reduction peaks, as indicated by an increased full width at half maximum (FWHM), suggests greater heterogeneity in gold crystal domains or the presence of undesired reactions, both of which can hinder the effective immobilization of sensing monolayers. In addition, the large ORR peak for RNB corresponds to a large ECSA, indicating a high density of available surface sites for molecular interactions (*31*). To capture this relationship quantitatively, we define a quality factor (Q) as

$$Q = \frac{I_{peak}}{FWHM} \quad (1)$$

where the I_{peak} is the reduction peak current. The RNB demonstrates a sharper ORR peak and high electrochemical quality (Fig. 2J).

Monolayer-based electrochemical sensing on RNB

To demonstrate the utility of the RNB for sensing molecules like therapeutic drugs, electrodes were functionalized with a methylene blue–tagged aptamer monolayer through covalent thiol bonding (*31*). This mechanism transduces target binding–induced aptamer conformational changes into electrochemical signals [retrievable using square wave voltammetry (SWV)], with methylene blue serving as a redox reporter (Fig. 2K). The reduction peak of methylene blue was used to construct calibration curves for sensor performance evaluation.

To illustrate the versatility of RNB-based aptamer sensors, four distinct aptamers, each with a dissociation constant (K_d) within physiologically relevant ranges, were used to target diverse molecules: vancomycin, irinotecan, and doxorubicin (antibiotics/chemotherapeutics with NTI) as well as phenylalanine (a biomarker for metabolic disorders like phenylketonuria) (Fig. 2, L and M, and fig. S8, A and B). The RNB sensor exhibited rapid and reversible response kinetics, stabilizing within two SWV scans (about 15 s) upon exposure to varying analyte concentrations (fig. S9).

Monolayer aptamer on the RNB surface was further quantified through chronocoulometry using hexaammineruthenium(III) chloride (RuHex) (fig. S10), yielding $2.6 \times 10^{12} \pm 0.8 \times 10^{12}$ receptor molecules/cm^2, consistent with reported well-packed monolayers on high-quality gold surfaces (*32*). Monolayer stability was further assessed using 10,000 consecutive SWV scans, during which RNB's signal performance matched that of standard planar gold-disc electrodes and outperformed nanoporous electrodes fabricated by conventional rushed dealloying (fig. S11).

RNB is also adaptable to various other reagent-free sensing mechanisms such as molecular pendulum and enzymatic and ion-selective sensing. We demonstrated this potential by fabricating RNB into the following: (i) a molecular-pendulum B-type natriuretic peptide (BNP) sensor operating at +0.5 V (versus Ag/AgCl) using a chronoamperometry technique (fig. S12, A to C), which produced concentration-dependent faraday current and a corresponding calibration response across a physiology-relevant BNP range; (ii) an electroenzymatic lactate sensor operating at +0.5 V (versus Ag/AgCl) using an amperometry technique (fig. S13, A and B), which showed a linear lactate-current calibration curve; and (iii) an ion-selective pH sensor under open-circuit potential conditions (fig. S13, C and D), which exhibited a linear pH-potential calibration curve over pH 5 to 9.

The RNB design enhanced the sensor SNR through multiple mechanisms. First, the RNB's ECSA was ~43 mm^2, which is 77 times the physical needle area, as measured by the surface gold oxide reduction peak height (fig. S14), providing a proportional increase in available recognition sites for enhanced signals. Comparison of vancomycin aptamer sensors with different electrodes further confirmed the RNB's superior SNR (Fig. 2N), consistent with its higher Q factor and effective monolayer immobilization.

Moreover, the RNB's nanocavity-textured surface enhanced analyte retention through Knudsen diffusion–like behavior while also shortening the Debye length for the redox reporter (*33*). We specifically confirmed Knudsen diffusion behavior by *b*-value analysis of freely moving methylene blue voltammograms (Fig. 2O) (*34*), where a *b*-value close to 1 for RNB indicates reaction-limited behavior due to strong surface confinement, in contrast with diffusion-limited systems like the disc electrode (*b*-value about 0.5; Fig. 2P). In addition, the surface produced by the SMD process improved methylene blue electron transfer kinetics (fig. S15A), as reflected in the reduced charge-transfer resistance (R_{CT}) derived from electrochemical impedance spectroscopy (fig. S15, B to D). These enhancements translated into improved sensitivity for RNB sensors (fig. S16).

Biofouling experiments in undiluted fetal bovine serum showed that traditional disc or nanodendritic electrodes suffered from signal degradation (Fig. 2Q and fig. S17). In contrast, RNB sensors displayed only a 20% signal reduction after 9 days of continuous operation, with no apparent sensitivity loss ($P > 0.05$) (fig. S18). The RNB's sub–50-nm nanoconcave geometry likely acts as a molecular sieve, blocking larger biomatrix species such as proteins while allowing small molecules to access the surface. This antifouling property reduces nonspecific binding to monolayer defect sites (*18*, *35*). The high SNR from a single RNB could enable reliable signal readout without multineedle arrays. Combined with our fabrication approach for individual sensor functionalization and monolithic patch integration, this architecture could enable multiplexing in a compact footprint (fig. S19).

RNB shows resilient in-tissue deployment

To evaluate the RNB's resilience in ISF in different tissues, we compared its ex vivo and in vivo performance with nanodendritic

electrodes (as a model nanostructured design) with matched surface area. Hydrogel-based artificial tissue (AT) models mimicking skin stiffness (Young's modulus $E = 180$ kPa) were used for ex vivo nanostructure mechanical characterization (Fig. 3A and fig. S20). Postinsertion optical microscopy revealed substantial debris from nanodendritic electrodes, indicating surface breakage, whereas the RNB left a clean, spotless pore (Fig. 3A, inset). Gold-debris quantification by inductively coupled plasma mass spectrometry showed more than 30 μg of gold debris shed from nanodendritic electrodes, compared with an undetectable amount for the RNB.

To provide a mechanistic understanding of these observations, we conducted finite element analysis, simulating stress distribution in embedded and extruded nanostructures under tissue contact (Fig. 3B, left) (*36*). Extruded structures experience sharp stress concentration at the base (quantified as ratio of maximum stress, σ_{max}, to average loading stress, σ_{load}), which increases with the height-to-diameter aspect ratio, compromising device mechanical integrity. In contrast, the RNB's embedded design minimizes stress concentration, even at higher depth-to-diameter aspect ratios used for surface area enhancement, ensuring structural integrity for reliable tissue deployment (Fig. 3, B and C).

To evaluate abrasion resistance, we repeatedly inserted aptamer sensors into AT models spanning a wide range of stiffnesses that covered the mechanical properties of soft biological tissues from 1 kPa to 1 MPa (Fig. 3, D to F). SEM analysis showed negligible morphological changes in the RNB after insertion in the ATs, and the RNB surface maintained its micrometer-scale smoothness (Fig. 3D). The RNB maintained functionality with minor detection signal loss (<5% after one insertion, 14% after 10 insertions at 930-kPa AT), whereas nanodendritic electrodes experienced 63% signal loss after a single insertion at 930-kPa AT (Fig. 3E). SEM showed that the nanodendritic electrodes had damage and detachment of their fractal structures, compromising their functionality (Fig. 3F). To evaluate long-term mechanical robustness, we conducted a 10,000 porcine-skin insertion cycle test for RNB. Posttesting characterization revealed no observable changes in electrode morphology or significant alteration ($P > 0.05$) in electrochemically active surface area (fig. S21, A to C), suggesting that the signal loss in Fig. 3E is primarily from partial monolayer detachment rather than electrode degradation. In addition, we assessed the sensor under dynamic motion by mounting RNB sensors on porcine skin and subjecting them to oscillatory movement simulating 1 week of human activity (>47,000 steps; peak acceleration, 10 m/s^2). The RNB exhibited minimal motion-induced artifacts (<2.5% signal drop) (fig. S22, A and B).

Next, we deployed the RNB sensors to measure vancomycin concentrations in excised tissues of varying stiffness (Fig. 3G) (*37*, *38*). The RNB sensor reliably detected increasing analyte concentrations, even in high-stiffness tissues like tendons (1 MPa), demonstrating RNB's resilience and broad applicability for monitoring analytes across diverse tissue environments (Fig. 3H). We compared the RNB microneedle sensor with a nanodendritic sensor targeting vancomycin in a rat with a single injection. The RNB sensor exhibited a 10-fold increase in faradaic current ($P < 0.001$) and effectively suppressed nonfaradaic contributions (fig. S23, A to C). These findings demonstrated the RNB's ability to protect monolayer-based sensing elements, thereby enabling high-SNR electrochemical monitoring in vivo.

Peripheral monitoring and data interpretation for drug clearance and organ function assessment

To evaluate the RNB's potential for reliable, minimally invasive TDM through in-skin analysis, we integrated the RNB sensor into a microneedle-based three-electrode system (aptamer-on-RNB working, Ag/AgCl reference, and gold counter electrodes), which can operate wirelessly through a Bluetooth-enabled potentiostat on a custom flexible printed circuit board (Fig. 4A and fig. S24, A to I). The wireless system's signal fidelity was validated by comparison with a commercial potentiostat (fig. S25), confirming in vivo signal acquisition capability.

To enhance data fidelity, we adapted the kinetic differential measurement (KDM) technique, which minimizes drift caused by biofouling, thermal desorption, and electrochemical instabilities (*39*). Traditional KDM based on fixed frequency pairs derived from in vitro studies does not accurately represent in vivo conditions. To address this, we developed a tKDM approach, selecting optimal frequency pairs through in vivo studies directly on the skin (Fig. 4B and fig. S26, A to F). These frequencies effectively cancel drift and were then used in subsequent in vivo PK studies. To further evaluate the generalizability of tKDM in different tissues, we implanted the RNB sensor into subcutaneous MC-38 tumors in mice (fig. S27, A to E). tKDM processing of RNB recordings at the in vivo preselected frequency pair accurately captured local drug kinetics [coefficient of determination (R^2) > 0.997], despite the distinct tissue characteristics of elevated interstitial pressure and a dense extracellular matrix.

To derive clinical insights from peripheral therapeutic data, we formulated an analytical framework that calculates PK parameters equivalent to blood-based TDM values. In short, following the two-compartment model (fig. S3), the peripherally recorded RNB sensor's response at time t postinjection is given by

$$R = Z \cdot \left(e^{-\beta t} - e^{-\alpha t}\right) \quad (2)$$

where Z, α, and β can be determined by regression fitting of the recorded signal. Extending the monitoring duration improves parameter extraction accuracy; with the RNB sensor's high SNR, less than 5% regression error can be achieved in just twice the time to peak (fig. S28).

The framework exploits a unified calibration factor U^*, combining device-concentration calibration with blood-to-ISF analyte conversion (k_{12}/k_{21}). U^* can be precharacterized with minimal blood sampling, for example, by measuring the ISF-to-blood drug concentration ratio at peak peripheral concentration (eq. S9). Using the precalibrated factor U^* and the real-time fitted parameters Z, α, and β, key PK parameters, such as half-life, total drug exposure, and clearance, can be derived from peripheral measurements (Fig. 4C).

Before in vivo application, the biocompatibility of the RNB sensor was confirmed using human dermal fibroblasts (HDFs), where cells maintained normal morphology and activity after 48 hours, showing no cytotoxicity (fig. S29A). Long-term testing over 7 days showed no significant changes ($P > 0.05$) in cell viability (fig. S29B), supporting suitability for extended biological contact.

The in vivo durability of the RNB microneedle was demonstrated by continuously tracking the daily vancomycin PK profile in a rat over 6 consecutive days ($R^2 = 0.93$ on day 6; Fig. 4D), with no observable electrode degradation upon explantation (fig. S30). The decrease of R^2 primarily originated from the elevated nonfaradaic background current in SWV, with a mild reduction in the aptamer peak, indicating a major loss of the passivation layer. These multiday

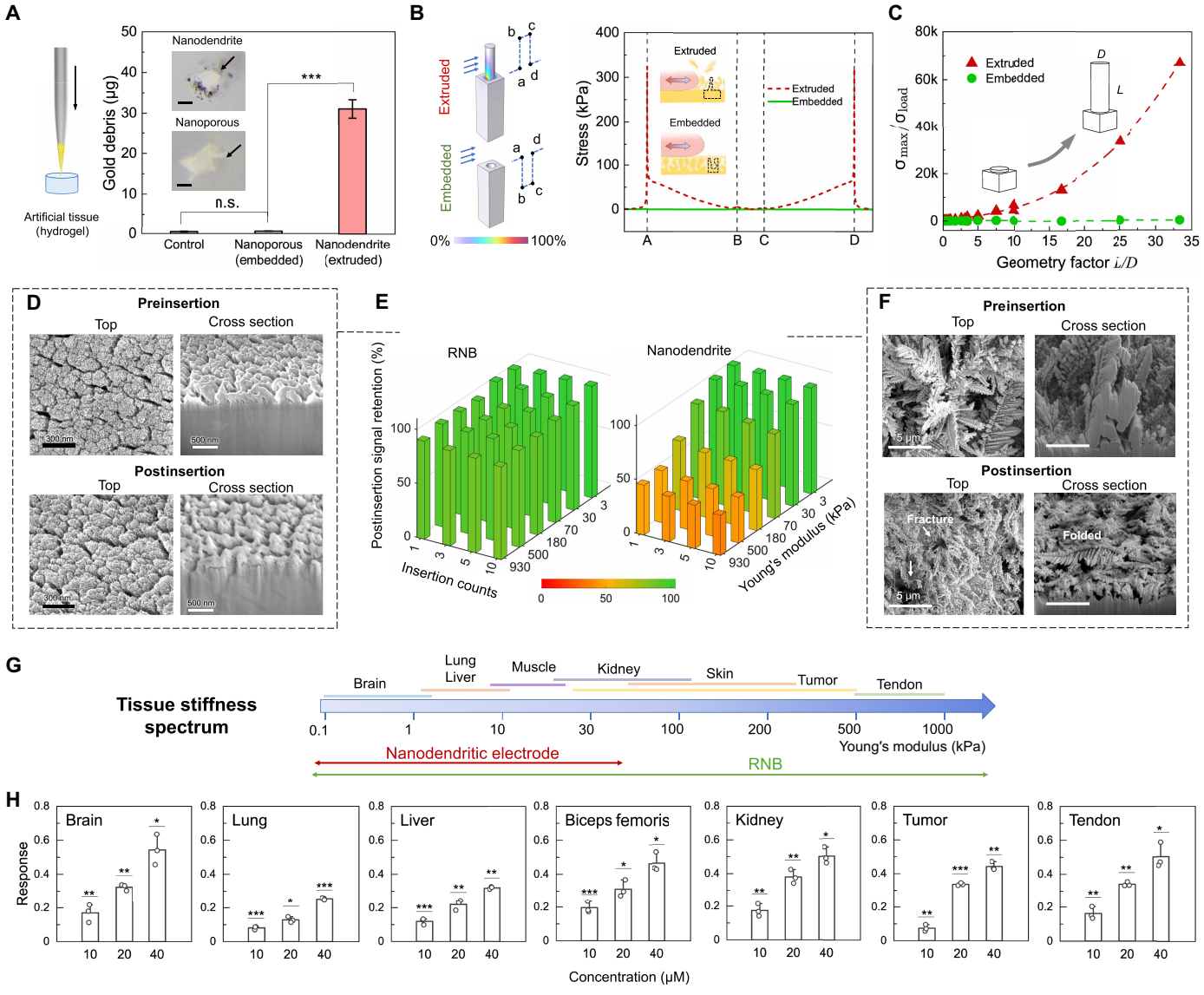

Fig. 3. Mechanical and electrochemical characterization of RNB's resilience for in-tissue deployment. (**A**) Illustration of the experimental setup used to test the nanostructured needles (left). Mass of gold debris (black) left inside the AT after a single insertion of three needles (right). Insets show optical images of the insertion sites. Scale bar, 1 mm. n.s., not significant. (**B**) Simulation results showing surface stress distribution in three-dimensional (3D) (left) and 2D along the center line (right). "a", "b", "c", and "d" indicate the labeled corners in (left). Inset schematic shows the protective effect of the nanoporous structure. (**C**) Stress concentration ratios for different geometric factors. (**D** to **F**) Characterization of sensors with different nanostructured surface designs. SEM morphology characterization of the RNB (D) and nanodendritic (F) electrodes preinsertion (top row) and postinsertion (bottom row) into the AT. Electrochemical characterization of signal retention after repeated insertions into the AT (E) ($n = 3$). (**G**) Spectrum of stiffness across various organs/tissues. The arrow at the bottom indicates the stiffness range in which the sensor retains 80% of its electrochemical signals after insertion. (**H**) Sensor response in different tissues with varying vancomycin concentrations. ***$P < 0.001$, **$P < 0.01$, and *$P < 0.05$; two-tailed, two-sample t tests.

results demonstrated the sustained high-SNR performance of the platform under prolonged implantation compared with previous research (table S2) (*10*, *16*, *18*, *21*, *22*, *40*–*44*).

The clinical utility of our solution was first validated for hepatic drug metabolism using irinotecan, a liver-metabolized chemotherapy drug with NTI, in both healthy and CCl_4-induced acute liver damage rats. Irinotecan is enzymatically hydrolyzed in the liver to produce its active metabolite, SN-38, which plays a central role in both its therapeutic effects and toxicity (*45*). Impaired liver function disrupts this process, delaying SN-38 formation and prolonging systemic exposure to both irinotecan and SN-38, potentially exacerbating side effects (Fig. 4E) (*3*, *46*). Histopathological analysis confirmed liver steatosis including fat vacuoles in centrilobular areas (Fig. 4F), and biochemical assays showed elevated serum alanine transaminase concentration in CCl_4-treated rats (fig. S31).

Peripheral irinotecan recordings from the RNB sensor (post–tail vein injection, 40 mg/kg) exhibited the characteristic drug distribution and redistribution/elimination phases in a healthy rat (Fig. 4G). Analysis of the peripherally fitted parameters indicated a prolonged half-life and impaired clearance of irinotecan in liver-damaged rats

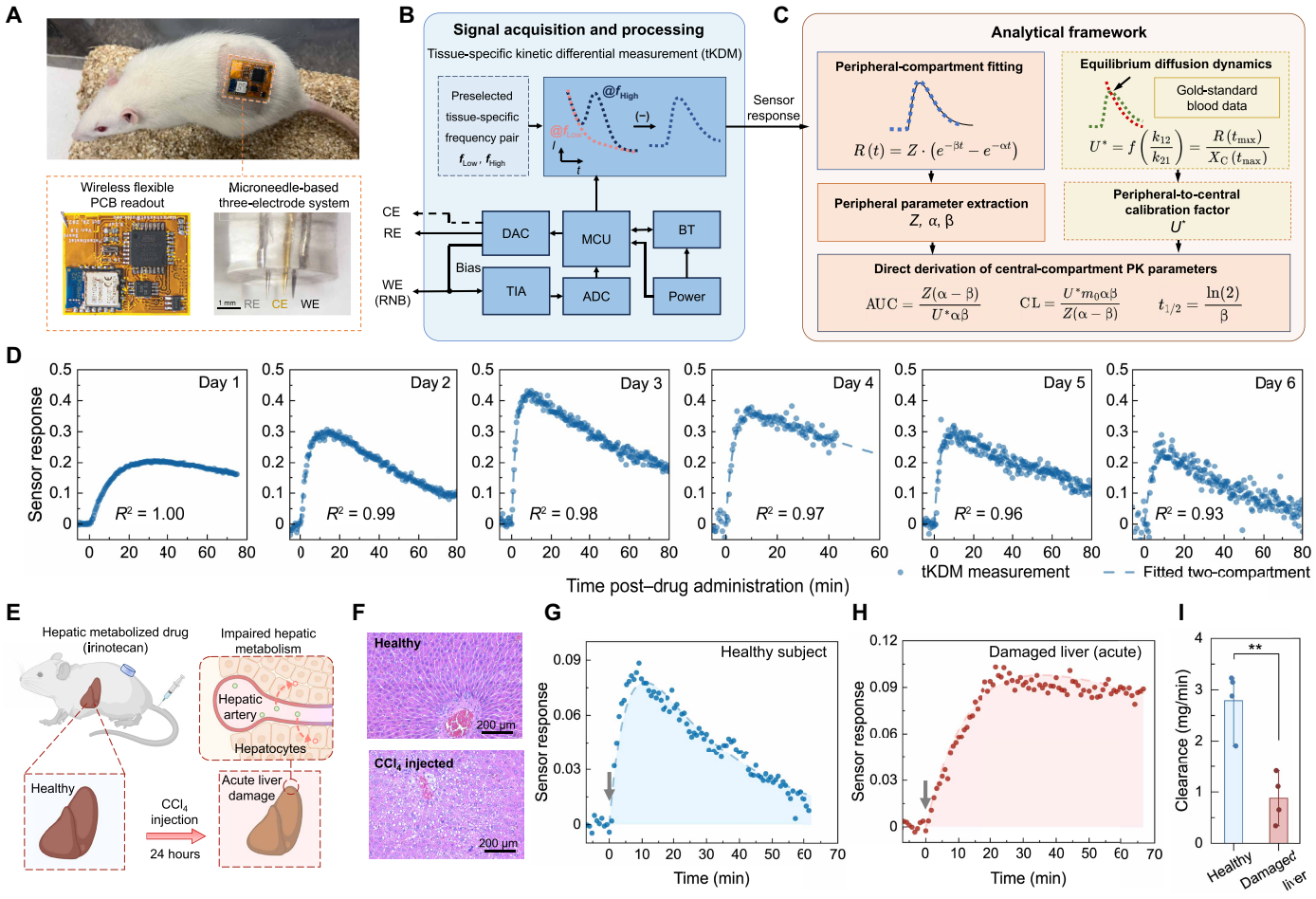

Fig. 4. Integrated wearable TDM device and hepatic clearance. (**A**) Integrated system for in vivo drug monitoring. Top: Photo of a rat carrying the circuit. Bottom: Photo of wireless flexible potentiostat circuit and microneedle-based three-electrode system (right). PCB, printed circuit board. (**B**) Signal acquisition and processing diagram blocks. The data retrieved by circuit are processed using tKDM for drift cancellation. DAC, digital to analog converter; MCU, microcontroller unit; BT, Bluetooth; TIA, transimpedance amplifier; ADC, analog to digital converter. (**C**) Analytical framework for sensor response interpretation, including data fitting and derivation of precalibration factor (U^*) from blood data. (**D**) Sensor response to daily vancomycin administration over 6 consecutive days (30 mg/kg per dose). The dashed line represents the fitted PK profile based on a two-compartment model (Eq. 2). (**E**) Experimental design for acute–liver damage induction and in vivo device validation. (**F**) H&E-stained images of rat liver without (top) and with (bottom) CCl_4 injection. (**G** and **H**) PK curve recordings of irinotecan in a healthy rat (G) and a rat with acute liver damage (H). Arrow indicates tail vein drug administration. The dashed line represents the fitted PK profile. (**I**) Sensor-derived PK parameter clearance for healthy and acute liver-damaged rats. $n = 4$, $^{**}P < 0.01$; two-tailed, two-sample t tests.

(Fig. 4, H and I, and fig. S32). These findings validate the RNB sensor's capability for real-time, minimally invasive monitoring of liver drug metabolism.

RNB performs drug-specific renal clearance monitoring and dysfunction detection in rats

Building on the potential of the RNB device and analytical framework, we investigated its utility for assessing renal clearance by deriving blood-equivalent PK parameters. Specifically, we conducted animal studies using vancomycin, a widely used renal metabolite NTI antibiotic that requires dose adjustment in patients with renal dysfunction (*47*). For benchmarking and calibration, we compared RNB-based peripheral recordings with two independent renal-function assessments: blood vancomycin concentration and key renal biomarkers [creatinine and blood urea nitrogen (BUN)], measured using established gold-standard blood test methods (*48*).

To evaluate the utility of our solution, we conducted two studies: one with healthy rats and varying dosing (study 1) and another with chronic kidney disease (CKD) models involving progression and recovery (study 2) (Fig. 5A). Both studies aimed to assess the reliability of the RNB sensor's peripheral recordings and the correlation between ISF- and blood-derived PK data. To examine the robustness of the bioanalytical framework across widely varied renal-function states, we applied the averaged calibration factor (U^*) from peak ISF equilibrium in study 1 to derive area under the curve (AUC) and clearance in both studies and compared these values with corresponding blood-derived parameters.

In study 1, vancomycin was administered in escalating doses (20 to 60 mg/kg, bolus injection) over 3 weeks to healthy rats (Fig. 5B). For each session, a new RNB sensor was applied and started measuring 30 min before drug administration in each rat. PK profiles from both ISF and blood followed the kinetic patterns predicted by

the two-compartment model and showed a dose-dependent increase in drug exposure (Fig. 5C and fig. S33). Total drug exposure derived from peripheral recordings, using the averaged calibration factor, demonstrated a strong linear correlation ($R^2 = 0.94$; fig. S34) and concordance across all dosages. The Bland-Altman analysis showed a minimal mean bias of −10.6 μM/hour, with all data points within the 95% limits of agreement (−66.9 to +45.6 μM/hour; Fig. 5D). These results supported the bioanalytic-RNB sensor's accuracy in capturing drug exposure trends and validated the precalibration strategy for the subsequent study.

Study 2 aimed to model two CKD-oriented scenarios: one involving progressive glomerular filtration rate (GFR) decline, characteristic of clinical renal dysfunction requiring close monitoring (*49*), and the other incorporating recovery, mimicking dynamic GFR fluctuations in response to therapeutic interventions like dialysis (*50*).

For the first scenario, the CKD model was induced by a high-adenine diet (Fig. 5E). The bioanalytic-RNB sensor detected a change in drug clearance after CKD induction, dropping from 3.67 to 0.35 ml/min by week 7, signaling progressive renal dysfunction (Fig. 5, F and G). This trend mirrored the blood-derived data and was corroborated by additional regression-based estimated GFR (eGFR) analysis (*48*). The corresponding renal biomarkers creatinine and BUN showed a consistent increase that agreed with ISF-derived clearance data (Fig. 5H), and histopathology showed progressive kidney damage, including cystic enlargement of kidney tubules and hematoxylin and eosin (H&E) staining (Fig. 5I). These results support the sensor's capability to monitor drug clearance in real time during renal dysfunction.

In the second scenario, rats were initially exposed to high-adenine diet for 2 weeks, followed by a normal diet supplemented with daily anti–uric acid therapy for 2 weeks (Fig. 5J). The clearance derived from the bioanalytic-RNB sensor showed a distinct decrease-then-increase during the high-adenine diet and subsequent intervention phase (Fig. 5, K and L). These changes mirrored the blood-derived trend and aligned with eGFR analyses, demonstrating the potential of the RNB sensor to inform real-time treatment decisions and provide insight into renal function and therapeutic outcomes.

Further analysis of our results revealed the sensor's potential for detecting early-stage kidney damage, a critical feature for timely intervention during antibiotic therapy (*47*). Specifically, during the first week after dietary changes, blood creatinine concentration remained below diagnostic thresholds and, together with peak blood vancomycin concentrations, showed no significant change (Fig. 5M and fig. S35; $P > 0.05$). However, bioanalytic-RNB measurements indicated a marked reduction in drug clearance (Fig. 5N), highlighting its greater sensitivity to early renal dysfunction compared with creatinine-based diagnostics. This difference can be attributed to creatinine's nonlinear clearance and its lag behind GFR changes (*51*, *52*), which make traditional assays less effective in detecting subtle alterations in the early stages of kidney impairment.

The collective results demonstrate the bioanalytic-RNB sensor's ability to accurately derive PK parameters, even amid major fluctuations in kidney function. This confirms the robustness of both the sensor and the bioanalytical framework, with the precalibration factor effectively translating from healthy rats to rats with varying CKD severities ($R^2 = 0.84$; Fig. 5O). These findings support the generalizability of the bioanalytic-RNB sensor for continuous, real-time drug clearance monitoring and supplemental organ function assessment across diverse physiologic states in preclinical models.

DISCUSSION

The wearable bioanalytic RNB minimal-invasively monitored circulating therapeutic drugs, derived PK parameters, and detected organ dysfunction on the basis of drug-specific clearance capacities earlier than standard assays. The nanocavity-textured design of the RNB ensures high SNR and mechanical and electrochemical resilience. These attributes are critical for reliable in-tissue analysis of low-concentration analytes, such as therapeutics, yet remain unaddressed by conventional microneedle devices. Integration into RNB can lower the translational barrier for the rich library of monolayer electrochemical biosensors, enhancing their in vivo potential, particularly those already proven effective for extended analyte monitoring in blood-based and other invasive methods (*53*). The RNB's expanded potential window, covering both negative and positive excitation voltages, broadens its versatility for electrochemical sensing, including molecular-pendulum sensing (*54*). Combined with the RNB's ability to achieve high SNR from a single needle (unlike microneedle use arrays for a single analyte) (*10*, *21*), this enables highly multiplexed analysis in a compact device. The RNB's mechanical robustness across a wide range of stiffnesses further extends its applicability for sensing in diverse body locations, including internal organs and lesions (*55*).

Beyond the device's robust in-tissue performance, the bioanalytical framework also plays a crucial role in interpreting peripheral measurements. A major advantage of this framework is the precalibration strategy using a unified, ratiometric-based calibration factor, which is generalizable to other drug administration routes. This strategy simplifies intercompartmental diffusion modeling and reduces common-mode confounding effects.

Despite these advances, several limitations remain before the RNB platform can be translated to clinical adoption. First, our in vivo validation relied on small-animal models with limited sample size. Second, we focused on vancomycin and irinotecan as representative NTI drug targets, which may not reflect blood-ISF partitioning and sensor performance characteristics for other therapeutics and biomarkers. Last, device miniaturization and integration have thus far relied on low-volume prototyping protocols. These limitations can be addressed through a staged, multifaceted strategy, encompassing engineering optimization, phased clinical studies, and alignment with regulatory and health care delivery frameworks.

From an engineering standpoint, future work should focus on enhancing the long-term stability of the sensing interface by using nonimmunogenic surface coatings (*56*), strengthening receptor immobilization through covalent bonding, and mitigating enzymatic degradation, such as through chemical modification of the receptor. Complementarily, implementing algorithmic and data-driven drift correction could further enhance signal fidelity during extended use (*57*).

Clinically, early-phase human studies are needed to assess safety and PK fidelity, with an initial focus on short-term monitoring applications like infusion centers. These studies should benchmark ISF-derived pharmacokinetics against clinical gold standards and validate the platform's ability to track systemic drug clearance and organ dysfunction under rigorous statistical modeling and agreement testing. Trials should include diverse patient

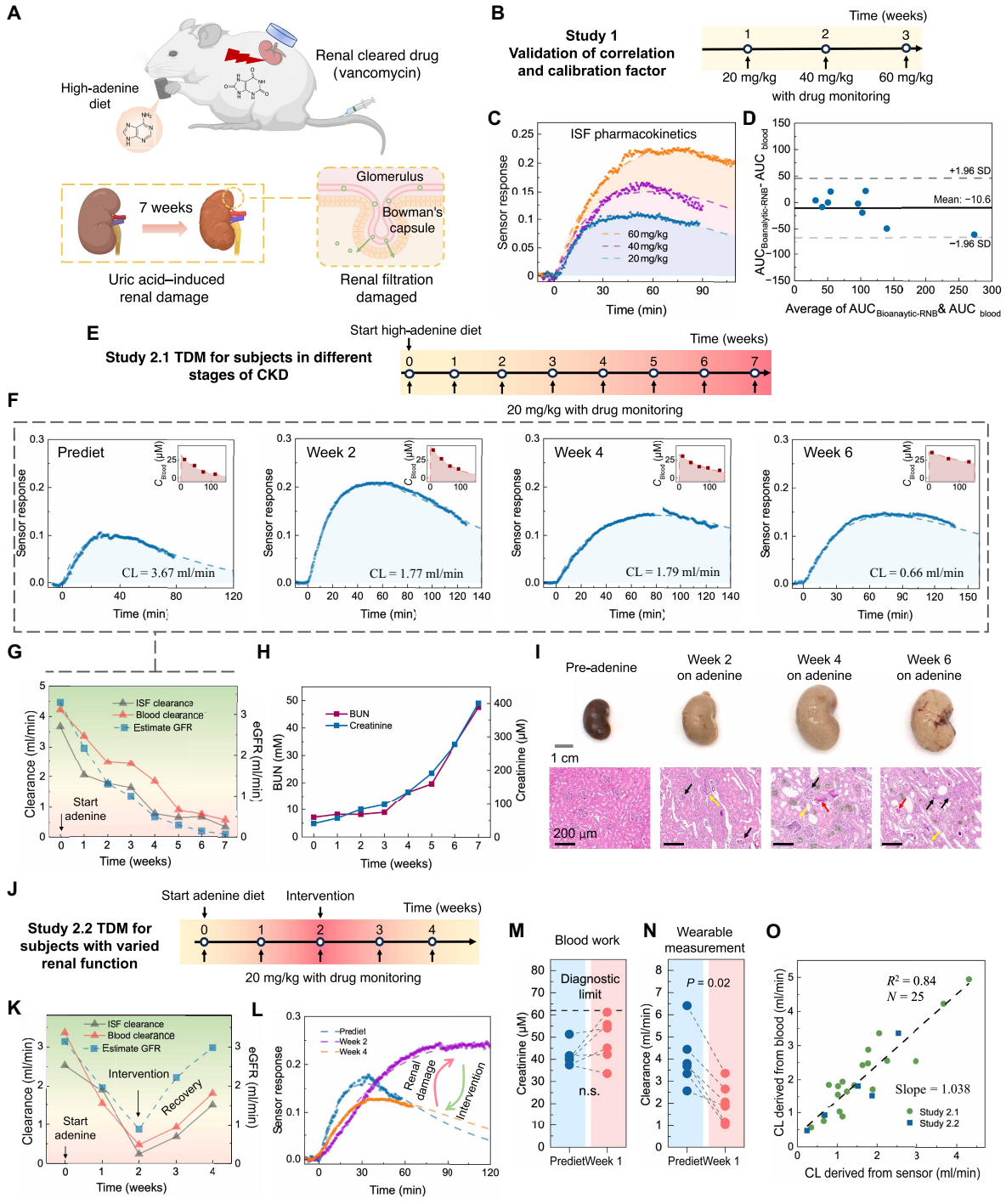

Fig. 5. Renal clearance quantification and early prediction. (**A**) Experimental design for chronic kidney damage. Created in part with BioRender.com. (**B**) Experimental timeline for study 1, treatment with indicated concentrations of vancomycin. (**C**) PK curves for different doses of vancomycin in a rat. (**D**) Bland-Altman plots comparing the bioanalytic-RNB–based AUC with the blood AUC (micromolar per hour). (**E**) Experimental timeline for animals with induction of progressive CKD by high-adenine diet and daily vancomycin treatment at 20 mg/kg. (**F**) ISF vancomycin PK curves at prediet and weeks 2, 4, and 6 on diet. The dashed line represents the fitted PK profile (Eq. 2). Insets show blood PK curves. (**G** and **H**) Changes in vancomycin clearance and eGFR (G) and BUN and serum creatinine concentration (H) over the 7-week study. (**I**) Top: Photos of kidneys at prediet and weeks 2, 4, and 6 on diet; bottom: H&E-stained kidney images showing white blood cell casts (yellow arrows), glomerular sac atrophy (black arrows), and inflammation (red arrows). (**J**) Experiment timeline for renal damage by high-adenine diet and intervention. Lower arrows indicate timing of vancomycin treatment and drug monitoring studies. (**K**) Changes in vancomycin clearance and eGFR for study 2.2. (**L**) Representative PK curve for a rat in the study 2.2. (**M**) Serum creatinine concentration after 1 week on a high-adenine diet ($n = 6$; n.s., nonstatistically significant with $P > 0.05$; two-tailed, paired t test). (**N**) Bioanalytic-RNB–based vancomycin clearance analysis shows a statistically significant reduction, indicating potential for early detection of renal impairment ($n = 6$, two-tailed, paired t tests). (**O**) Correlation of the drug clearances between the RNB bioanalytical method using the device and blood quantification in studies 2.1 and 2.2. CL, clearance.

groups, spanning age, sex, renal and hepatic functions, and comorbidities, to assess the generalizability of U^*, establish actionable readout thresholds, and evaluate the clinical decision-making utility of the platform.

Upon successful validation, the platform can be deployed in settings where real-time dose adjustment is critical, such as infectious disease and critical care. For example, for the model analyte targeted here, it could help prevent vancomycin-induced acute kidney injury [~35% of patients on combination antibiotic therapy (*47*, *49*)] or irinotecan-induced neutropenia [about 30% of patients (*58*)]. Compared with liquid chromatography–mass spectrometry (LC-MS), the RNB provides real-time, point-of-care insights without requiring centralized labs, trained phlebotomists, or batch processing, substantially reducing turnaround time and access barriers, especially in decentralized or resource-limited settings (*59, 60*). In the near term, the device use could follow a postdeployment calibration model, using a single-point reference, similar to earlier commercial continuous glucose monitors (CGMs) (*61*). As more real-world data accumulate, specialized algorithms and patient-specific models may enable calibration-free sensing, as seen in next-generation CGMs. For manufacturing and regulatory readiness, the key fabrication steps are compatible with wafer-scale batch processing and standard biosensor manufacturing tools, enabling mass production at low material cost [<$1.50 per sensor, 1% of the cost of a typical vancomycin TDM panel (*62*); table S1]. The platform's compatibility with wireless, flexible electronics integration and overall self-deployability further support scalable deployment. Together, these advances establish the RNB as a versatile platform for generating real-time molecular insights into localized and systemic processes, opening avenues to unravel complex biology, accelerate therapeutic development, and deliver personalized precision care.

MATERIALS AND METHODS

Study design

The objective of this study was to develop and demonstrate a bioanalytical device for minimally invasive TDM and associated drug-specific organ function assessment. Our study consisted of two major parts: electrode and sensor fabrication and characterization (electrode failure mode, sensor functionality and performance, mechanical robustness, and biocompatibility) and in vivo animal pharmacokinetics and disease model validation. For in vitro characterization, dynamic response of aptamer sensors (targeting vancomycin and irinotecan) was validated in buffer using SWV, and mechanical stability was tested using agarose hydrogels (0.2 to 10 wt %), porcine skin, and finite element modeling of nanostructures. Device biocompatibility was evaluated by in vitro culture with HDFs. For in vivo validation, microneedle sensor was applied to Sprague-Dawley rats for continuous TDM sessions [healthy animal, CCl_4-induced liver injury, and adenine diet–induced kidney failure, under University of California, Los Angeles (UCLA)–approved protocols ARC-2021-011 and ARC-2023-114]. For long-term in vivo sensor validation, integrated microneedle device without circuit was applied and fixed on the dorsal side of a rat, and vancomycin TDM was performed every day until no SWV peak was retrievable. For bioanalytical TDM experiments in healthy and organ-impaired subjects, the disease is induced by CCl_4 injection or a high-adenine diet. CCl_4 induces liver injury by centrilobular necrosis, oxidative stress, and impaired phase I/II metabolism, thereby closely modeling human drug-induced hepatotoxicity (*63*). Similarly, low-dose adenine forms renal precipitates that trigger fibrosis, reduced filtration, and uremia, recapitulating human CKD pathology (*64*). For vancomycin-based TDM and renal-function assessment, sensor results were then correlated with LC–tandem MS serum analysis using serum samples collected concurrently during the TDM sessions for analysis. In a separate experiment to validate tKDM in tumor tissue, the vancomycin microneedle sensor was implanted into dorsal tumor tissue (murine colon adenocarcinoma cells MC-38) in a female C57BL/6 J mouse, under UCLA-approved protocol ARC-2017-072. No data were excluded from the analyses. The animal experiments were not blinded, and sample sizes are stated in the figure captions and determined on the basis of previous publication. Randomization was not applicable for this study.

Electrode fabrication

The RNB was fabricated from gold-plated acupuncture needles, and all electrochemical measurements were performed using a CHI660E or CHI1040C workstation (CH Instruments). Needles were cleaned by sonication in acetone, ethanol, and high-performance liquid chromatography (HPLC)–grade water (5 min each). To form a thick, homogeneous adhesion layer, gold was electrodeposited from Elevate Gold 7990 at 65°C by applying −0.75 V (versus Ag/AgCl) for 10 s followed by −0.5 V for 20 min under stirring. After rinsing with HPLC water, a 30-nm Au layer and a 300-nm Ag:Au alloy layer (2:1) were deposited by sputtering. Conventional heterogeneous-adhesion coating was prepared by plasma treatment followed by deposition of 50-nm Ti, 30-nm Au, and 300-nm 2:1 Ag:Au alloy using the same sputtering system.

To generate nanoporous gold, Ag was dealloyed using a SMD process in 50 mM H_2SO_4 via linear sweep voltammetry from 0.3 to 1.2 V at 5 mV s^{-1}, followed by CV in the same electrolyte over 0.2 to 1.35 V for 5 cycles at 100 mV s^{-1}. Electrodes were then rinsed with deionized water before surface characterization or functionalization. The exposed needle length was defined by applying a polytetrafluoroethylene heat-shrink tube (0.018 in diameter; Zeus Industrial Products) or polydimethylsiloxane before dealloying.

Sensor fabrication

To construct the aptamer sensor, 5 μl of 100 μM thiolated methylene blue–DNA aptamer was reduced with 10 μl of tris(2-carboxyethyl) phosphine hydrochloride (TCEP) for 1 hour in the dark. TCEP concentration was tuned by aptamer to optimize probe density, with higher TCEP generally yielding higher surface density: 10 mM TCEP was used for tobramycin, phenylalanine, and irinotecan aptamers, whereas 100 mM TCEP was used for the vancomycin aptamer. TCEP was prepared in buffer containing 100 mM tris-HCl, 140 mM NaCl, 20 mM $MgCl_2$, and 20 mM KCl (pH 7.4). The reduced aptamer solution was diluted with 500 μl of PBS, and the RNB was incubated in this solution for 2 hours at room temperature in the dark to immobilize DNA. After immobilization, sensors were passivated in 20 mM 6-mercapto-1-hexanol (in PBS) overnight at room temperature, rinsed with water, and used for testing. The DNA sequence used for the construction of the sensor is listed as follows: Vancomycin: 5′-/5ThioMC6-D/CGAGGGTACCGCAATAGTACTTATTGTTCGCCTATTGTGGGTCGG/3MeBlN/-3′, doxorubicin: 5′-/5ThioMC6-D/ACCATCTGTGTAAGGGGTAAGGGGTGGT/3MeBlN/-3′, phenylalanine: 5′-/5ThioMC6-D/CGACCGCGTTTCCCAAGAAAGCAAGTATTGGTTGGTCG /3MeBlN/-3′, and irinotecan:

5′-/5ThioMC6-D/TCCGGACTTGGGTGGGTGGGTTGGGGTACGGT/3MeBlN/-3′.

In vivo rat test

All rat TDM studies were conducted under protocols approved by the UCLA Institutional Animal Care and Use Committee. Mixed-sex Sprague-Dawley rats (200 to 670 g; Charles River Laboratories) were housed in climate-controlled facilities on a 12-hour light/dark cycle with food and water provided ad libitum and were acclimated for at least 7 days before any experimental procedures. Sensors were removed after each TDM session except in multiday sensing experiments.

For continuous irinotecan monitoring, rats were anesthetized with inhaled isoflurane (3 to 5% induction, 1.5 to 2.5% maintenance) and placed on a circulating water-heated pad to maintain body temperature. After shaving the lower back, an RNB device was applied and interrogated by SWV using preoptimized parameters to obtain real-time tKDM readouts (10 and 150 Hz). Once the tKDM signal stabilized, baseline blood was collected by tail prick; samples were allowed to rest for 15 min and centrifuged for 10 min at 10,000 rpm, and serum was collected and stored at −20°C for analysis. Irinotecan (40 mg kg^{-1}) was then administered intravenously via the tail vein. In a separate cohort, acute liver injury was induced by carbon tetrachloride, and the same TDM and predose blood collection procedures were performed before irinotecan administration.

For long-term in vivo TDM, rats were anesthetized as above, and a vancomycin microneedle sensing device (without the circuit board) was applied to the upper back and secured with Vetbond (3M). Daily TDM measurements were performed at a fixed vancomycin dose (30 mg kg^{-1}) using an SWV frequency pair of 25 and 150 Hz. After each measurement, the sensor and attached flexible lead were covered with a small Tegaderm dressing. Measurements were repeated daily through day 7, when no discernible SWV peak could be recovered; no excessive stress or weight loss was observed during the study.

Statistical analyses

Statistical analyses were conducted using MATLAB (version 2023a). Data were assumed to be normally distributed but were not statistically tested for normality. Pearson correlation analyses were performed to assess the correlation between variables. Comparisons between two independent groups (for instance, RNB versus nanodendritic electrodes in fouling resistance) were analyzed using two-tailed unpaired Student's *t* tests. Paired Student's *t* tests were used to compare changes within the same electrode or subject. One-way analysis of variance (ANOVA) was used for analyzing three or more groups. All tests assumed a two-tailed hypothesis, with a significance level of $\alpha = 0.05$. Replication conditions for each experiment were defined and described in Results and figure captions, with all tests including at least three replicates unless noted in the text. All individual-level tabular data are included in data file S1.

Supplementary Materials

The PDF file includes:
Materials and Methods
Figs. S1 to S35
Tables S1 and S2

Other Supplementary Material for this manuscript includes the following:
Data file S1
Movie S1
MDAR Reproducibility Checklist

REFERENCES AND NOTES

1. V. Gambardella, N. Tarazona, J. M. Cejalvo, P. Lombardi, M. Huerta, S. Roselló, T. Fleitas, D. Roda, A. Cervantes, Personalized medicine: Recent progress in cancer therapy. *Cancers* **12**, 1009 (2020).
2. S. G. Wicha, A.-G. Märtson, E. I. Nielsen, B. C. P. Koch, L. E. Friberg, J.-W. Alffenaar, I. K. Minichmayr, International Society of Anti-Infective Pharmacology (ISAP), the PK/PD study group of the European Society of Clinical Microbiology, Infectious Diseases (EPASG), From therapeutic drug monitoring to model-informed precision dosing for antibiotics. *Clin. Pharmacol. Ther.* **109**, 928–941 (2021).
3. F. M. de Man, A. K. L. Goey, R. H. N. van Schaik, R. H. J. Mathijssen, S. Bins, Individualization of irinotecan treatment: A review of pharmacokinetics, pharmacodynamics, and pharmacogenetics. *Clin. Pharmacokinet.* **57**, 1229–1254 (2018).
4. T. Nolin, J. Naud, F. Leblond, V. Pichette, Emerging evidence of the impact of kidney disease on drug metabolism and transport. *Clin. Pharmacol. Ther.* **83**, 898–903 (2008).
5. R. K. Verbeeck, Pharmacokinetics and dosage adjustment in patients with hepatic dysfunction. *Eur. J. Clin. Pharmacol.* **64**, 1147–1161 (2008).
6. F. de Velde, J. W. Mouton, B. C. M. de Winter, T. van Gelder, B. C. P. Koch, Clinical applications of population pharmacokinetic models of antibiotics: Challenges and perspectives. *Pharmacol. Res.* **134**, 280–288 (2018).
7. J. P. Cerdeña, M. V. Plaisime, J. Tsai, From race-based to race-conscious medicine: How anti-racist uprisings call us to act. *Lancet* **396**, 1125–1128 (2020).
8. A. Chapron, D. D. Shen, B. R. Kestenbaum, C. Robinson-Cohen, J. Himmelfarb, C. K. Yeung, Does secretory clearance follow glomerular filtration rate in chronic kidney diseases? Reconsidering the intact nephron hypothesis. *Clin. Transl. Sci.* **10**, 395–403 (2017).
9. L. K. Vora, A. H. Sabri, P. E. McKenna, A. Himawan, A. R. J. Hutton, U. Detamornrat, A. J. Paredes, E. Larrañeta, R. F. Donnelly, Microneedle-based biosensing. *Nat. Rev. Bioeng.* **2**, 64–81 (2024).
10. F. Tehrani, H. Teymourian, B. Wuerstle, J. Kavner, R. Patel, A. Furmidge, R. Aghavali, H. Hosseini-Toudeshki, C. Brown, F. Zhang, K. Mahato, Z. Li, A. Barfidokht, L. Yin, P. Warren, N. Huang, Z. Patel, P. P. Mercier, J. Wang, An integrated wearable microneedle array for the continuous monitoring of multiple biomarkers in interstitial fluid. *Nat. Biomed. Eng.* **6**, 1214–1224 (2022).
11. M. Friedel, I. A. P. Thompson, G. Kasting, R. Polsky, D. Cunningham, H. T. Soh, J. Heikenfeld, Opportunities and challenges in the diagnostic utility of dermal interstitial fluid. *Nat. Biomed. Eng.* **7**, 1541–1555 (2023).
12. N. Arroyo-Currás, J. Somerson, P. A. Vieira, K. L. Ploense, T. E. Kippin, K. W. Plaxco, Real-time measurement of small molecules directly in awake, ambulatory animals. *Proc. Natl. Acad. Sci. U.S.A.* **114**, 645–650 (2017).
13. J. Heikenfeld, A. Jajack, B. Feldman, S. W. Granger, S. Gaitonde, G. Begtrup, B. A. Katchman, Accessing analytes in biofluids for peripheral biochemical monitoring. *Nat. Biotechnol.* **37**, 407–419 (2019).
14. J. B. Chen, H. Yousefi, C. R. Nemr, S. Gomis, R. Atwal, M. Labib, E. Sargent, S. O. Kelley, Nanostructured architectures for biomolecular detection inside and outside the cell. *Adv. Funct. Mater.* **30**, 1907701 (2020).
15. F. Keyvani, H. Zheng, M. R. Kaysir, D. F. Mantaila, P. Ghavami Nejad, F. A. Rahman, J. Quadrilatero, D. Ban, M. Poudineh, A hydrogel microneedle assay combined with nucleic acid probes for on-site detection of small molecules and proteins. *Angew. Chem. Int. Ed.* **62**, e202301624 (2023).
16. S. Lin, X. Cheng, J. Zhu, B. Wang, D. Jelinek, Y. Zhao, T.-Y. Wu, A. Horrillo, J. Tan, J. Yeung, W. Yan, S. Forman, H. A. Coller, C. Milla, S. Emaminejad, Wearable microneedle-based electrochemical aptamer biosensing for precision dosing of drugs with narrow therapeutic windows. *Sci. Adv.* **8**, eabq4539 (2022).
17. C. Tortolini, A. E. G. Cass, R. Pofi, A. Lenzi, R. Antiochia, Microneedle-based nanoporous gold electrochemical sensor for real-time catecholamine detection. *Microchim. Acta* **189**, 180 (2022).
18. J.-W. Seo, K. Fu, S. Correa, M. Eisenstein, E. A. Appel, H. T. Soh, Real-time monitoring of drug pharmacokinetics within tumor tissue in live animals. *Sci. Adv.* **8**, eabk2901 (2022).
19. X. Xiao, P. Si, E. Magner, An overview of dealloyed nanoporous gold in bioelectrochemistry. *Bioelectrochemistry* **109**, 117–126 (2016).
20. E. Seker, M. L. Reed, M. R. Begley, Nanoporous gold: Fabrication, characterization, and applications. *Materials* **2**, 2188–2215 (2009).
21. Y. Wu, F. Tehrani, H. Teymourian, J. Mack, A. Shaver, M. Reynoso, J. Kavner, N. Huang, A. Furmidge, A. Duvvuri, Y. Nie, L. M. Laffel, F. J. I. Doyle, M.-E. Patti, E. Dassau, J. Wang, N. Arroyo-Currás, Microneedle aptamer-based sensors for continuous, real-time therapeutic drug monitoring. *Anal. Chem.* **94**, 8335–8345 (2022).

22. M. Reynoso, A.-Y. Chang, Y. Wu, R. Murray, S. Suresh, Y. Dugas, J. Wang, N. Arroyo-Currás, 3D-printed, aptamer-based microneedle sensor arrays using magnetic placement on live rats for pharmacokinetic measurements in interstitial fluid. *Biosens. Bioelectron.* **244**, 115802 (2024).
23. M. C. Dixon, T. A. Daniel, M. Hieda, D. M. Smilgies, M. H. W. Chan, D. L. Allara, Preparation, structure, and optical properties of nanoporous gold thin films. *Langmuir* **23**, 2414–2422 (2007).
24. W. Giurlani, L. Sergi, E. Crestini, N. Calisi, F. Poli, F. Soavi, M. Innocenti, Electrochemical stability of steel, Ti, and Cu current collectors in water-in-salt electrolyte for green batteries and supercapacitors. *J. Solid State Electrochem.* **26**, 85–95 (2022).
25. D. Kang, F. Ricci, R. J. White, K. W. Plaxco, Survey of redox-active moieties for application in multiplexed electrochemical biosensors. *Anal. Chem.* **88**, 10452–10458 (2016).
26. S. Trasatti, O. A. Petrii, Real surface area measurements in electrochemistry. *Pure Appl. Chem.* **63**, 711–734 (1991).
27. L. L. Martínez, M. Segarra, M. Fernández, F. Espiell, Kinetics of the dissolution of pure silver and silver-gold alloys in nitric acid solution. *Metall. Trans. B* **24**, 827–837 (1993).
28. S. Parida, D. Kramer, C. A. Volkert, H. Rösner, J. Erlebacher, J. Weissmüller, Volume change during the formation of nanoporous gold by dealloying. *Phys. Rev. Lett.* **97**, 035504 (2006).
29. J. Erlebacher, M. J. Aziz, A. Karma, N. Dimitrov, K. Sieradzki, Evolution of nanoporosity in dealloying. *Nature* **410**, 450–453 (2001).
30. W.-Y. Tsai, P.-L. Taberna, P. Simon, Electrochemical quartz crystal microbalance (EQCM) study of ion dynamics in nanoporous carbons. *J. Am. Chem. Soc.* **136**, 8722–8728 (2014).
31. M. A. Pellitero, A. Shaver, N. Arroyo-Currás, Critical review—Approaches for the electrochemical interrogation of DNA-based sensors: A critical review. *J. Electrochem. Soc.* **167**, 037529 (2019).
32. R. Lao, S. Song, H. Wu, L. Wang, Z. Zhang, L. He, C. Fan, Electrochemical interrogation of DNA monolayers on gold surfaces. *Anal. Chem.* **77**, 6475–6480 (2005).
33. K. Fu, J.-W. Seo, V. Kesler, N. Maganzini, B. D. Wilson, M. Eisenstein, B. Murmann, H. T. Soh, Accelerated electron transfer in nanostructured electrodes improves the sensitivity of electrochemical biosensors. *Adv. Sci.* **8**, e2102495 (2021).
34. C. Choi, D. S. Ashby, D. M. Butts, R. H. DeBlock, Q. Wei, J. Lau, B. Dunn, Achieving high energy density and high power density with pseudocapacitive materials. *Nat. Rev. Mater.* **5**, 5–19 (2020).
35. P. Daggumati, Z. Matharu, L. Wang, E. Seker, Biofouling-resilient nanoporous gold electrodes for DNA sensing. *Anal. Chem.* **87**, 8618–8622 (2015).
36. D. J. van Gerwen, J. Dankelman, J. J. van den Dobbelsteen, Needle–tissue interaction forces—A survey of experimental data. *Med. Eng. Phys.* **34**, 665–680 (2012).
37. C. F. Guimarães, L. Gasperini, A. P. Marques, R. L. Reis, The stiffness of living tissues and its implications for tissue engineering. *Nat. Rev. Mater.* **5**, 351–370 (2020).
38. C. T. McKee, J. A. Last, P. Russell, C. J. Murphy, Indentation versus tensile measurements of Young's modulus for soft biological tissues. *Tissue Eng. Part B Rev.* **17**, 155–164 (2011).
39. A. Shaver, N. Arroyo-Currás, The challenge of long-term stability for nucleic acid-based electrochemical sensors. *Curr. Opin. Electrochem.* **32**, 100902 (2022).
40. H. Zargartalebi, S. Mirzaie, A. GhavamiNejad, S. U. Ahmed, F. Esmaeili, A. Geraili, C. D. Flynn, D. Chang, J. Das, A. Abdrabou, E. H. Sargent, S. O. Kelley, Active-reset protein sensors enable continuous in vivo monitoring of inflammation. *Science* **386**, 1146–1153 (2024).
41. M. Friedel, B. Werbovetz, A. Drexelius, Z. Watkins, A. Bali, K. W. Plaxco, J. Heikenfeld, Continuous molecular monitoring of human dermal interstitial fluid with microneedle-enabled electrochemical aptamer sensors. *Lab Chip* **23**, 3289–3299 (2023).
42. J. Gerson, M. K. Erdal, M. H. McDonough, K. L. Ploense, P. Dauphin-Ducharme, K. M. Honeywell, K. K. Leung, N. Arroyo-Curras, J. M. Gibson, N. A. Emmons, W. Meiring, J. P. Hespanha, K. W. Plaxco, T. E. Kippin, High-precision monitoring of and feedback control over drug concentrations in the brains of freely moving rats. *Sci. Adv.* **9**, eadg3254 (2023).
43. F. Keyvani, P. GhavamiNejad, M. A. Saleh, M. Soltani, Y. Zhao, S. Sadeghzadeh, A. Shakeri, P. Chelle, H. Zheng, F. A. Rahman, S. Mahshid, J. Quadrilatero, P. P. N. Rao, A. Edginton, M. Poudineh, Integrated electrochemical aptamer biosensing and colorimetric pH monitoring via hydrogel microneedle assays for assessing antibiotic treatment. *Adv. Sci.* **11**, e2309027 (2024).
44. A. M. Downs, J. Gerson, M. N. Hossain, K. Ploense, M. Pham, H.-B. Kraatz, T. Kippin, K. W. Plaxco, Nanoporous gold for the miniaturization of in vivo electrochemical aptamer-based sensors. *ACS Sens.* **6**, 2299–2306 (2021).
45. G. G. Chabot, Clinical pharmacokinetics of irinotecan. *Clin. Pharmacokinet.* **33**, 245–259 (1997).
46. U. Vanhoefer, A. Harstrick, W. Achterrath, S. Cao, S. Seeber, Y. M. Rustum, Irinotecan in the treatment of colorectal cancer: Clinical overview. *J. Clin. Oncol.* **19**, 1501–1518 (2001).
47. S. Elyasi, H. Khalili, S. Dashti-Khavidaki, A. Mohammadpour, Vancomycin-induced nephrotoxicity: Mechanism, incidence, risk factors and special populations. A literature review. *Eur. J. Clin. Pharmacol.* **68**, 1243–1255 (2012).
48. P. J. Besseling, T. T. Pieters, I. T. N. Nguyen, P. M. de Bree, N. Willekes, A. H. Dijk, D. M. Bovée, E. J. Hoorn, M. B. Rookmaaker, K. G. Gerritsen, M. C. Verhaar, H. Gremmels, J. A. Joles, A plasma creatinine- and urea-based equation to estimate glomerular filtration rate in rats. *Am. J. Physiol. Renal Physiol.* **320**, F518–F524 (2021).
49. N. Hodoshima, S. Masuda, K. Inui, Decreased renal accumulation and toxicity of a new VCM formulation in rats with chronic renal failure. *Drug Metab. Pharmacokinet.* **22**, 419–427 (2007).
50. V. Launay-Vacher, H. Izzedine, L. Mercadal, G. Deray, Clinical review: Use of vancomycin in haemodialysis patients. *Crit. Care* **6**, 313–316 (2002).
51. C. L. Edelstein, *Biomarkers of Kidney Disease* (Academic Press, ed. 2, 2016).
52. L. A. Inker, S. Titan, Measurement and estimation of GFR for use in clinical practice: Core curriculum 2021. *Am. J. Kidney Dis.* **78**, 736–749 (2021).
53. C. D. Flynn, D. Chang, A. Mahmud, H. Yousefi, J. Das, K. T. Riordan, E. H. Sargent, S. O. Kelley, Biomolecular sensors for advanced physiological monitoring. *Nat. Rev. Bioeng.* **1**, 560–575 (2023).
54. J. Das, S. Gomis, J. B. Chen, H. Yousefi, S. Ahmed, A. Mahmud, W. Zhou, E. H. Sargent, S. O. Kelley, Reagentless biomolecular analysis using a molecular pendulum. *Nat. Chem.* **13**, 428–434 (2021).
55. N. Brasier, H. C. Ates, J. R. Sempionatto, M. O. Cotta, A. F. Widmer, J. Eckstein, J. Goldhahn, J. A. Roberts, W. Gao, C. Dincer, A three-level model for therapeutic drug monitoring of antimicrobials at the site of infection. *Lancet Infect. Dis.* **23**, e445–e453 (2023).
56. N. Li, S. Kang, Z. Liu, S. Wai, Z. Cheng, Y. Dai, A. Solanki, S. Li, Y. Li, J. Strzalka, M. J. V. White, Y.-H. Kim, B. Tian, J. A. Hubbell, S. Wang, Immune-compatible designs of semiconducting polymers for bioelectronics with suppressed foreign-body response. *Nat. Mater.* **25**, 124–132 (2026).
57. T. P. Engelhardt, N. Schmitt, P. E. Pash, D. Duke, A. Soni, Calibration of a handheld diabetes managing device that receives data from a continuous glucose monitor, US Patent US8589106B2 (2013); https://patents.google.com/patent/US8589106B2/en.
58. G. H. Lyman, Impact of chemotherapy dose intensity on cancer patient outcomes. *J. Natl. Compr. Canc. Netw.* **7**, 99–108 (2009).
59. R. H. Mathijssen, R. J. van Alphen, J. Verweij, W. J. Loos, K. Nooter, G. Stoter, A. Sparreboom, Clinical pharmacokinetics and metabolism of irinotecan (CPT-11). *Clin. Cancer Res.* **7**, 2182–2194 (2001).
60. G. R. Matzke, G. G. Zhanel, D. R. P. Guay, Clinical pharmacokinetics of vancomycin. *Clin. Pharmacokinet.* **11**, 257–282 (1986).
61. U. Hoss, E. S. Budiman, Factory-calibrated continuous glucose sensors: The science behind the technology. *Diabetes Technol. Ther.* **19**, S44–S50 (2017).
62. B. O. M. Claus, D. De Smedt, P. A. De Cock, Therapeutic drug monitoring versus Bayesian AUC-based dosing for vancomycin in routine practice: A cost–benefit analysis. *J. Antimicrob. Chemother.* **80**, 857–867 (2025).
63. L. W. D. Weber, M. Boll, A. Stampfl, Hepatotoxicity and mechanism of action of haloalkanes: Carbon tetrachloride as a toxicological model. *Crit. Rev. Toxicol.* **33**, 105–136 (2003).
64. V. Diwan, A. Mistry, G. Gobe, L. Brown, Adenine-induced chronic kidney and cardiovascular damage in rats. *J. Pharmacol. Toxicol. Methods* **68**, 197–207 (2013).

Acknowledgments: We appreciate the members of the University of California, Los Angeles, Nanoelectronics Research Facility for help in microfabrication/characterization. We extend our gratitude to B. Dunn for support of electrochemistry characterization and insightful discussions; P. Chen for guidance on the animal experiment and sample processing; California NanoSystems Institute staff member H. Q. Ngo; and Electron Imaging Center for Nanosystems staff members for fabrication and characterization support. **Funding:** This work was supported by Elisabeth K. Harris Foundation Trust (to S.E.); Cystic Fibrosis Foundation grant 003305G221 (to S.E.); Noble Family Innovation Fund granted by California NanoSystems Institute (to S.E.), 3Rs Grant; UCLA Vice Chancellor for Research and Creative Activities (to S.E.); National Institutes of Health grant R01 DK077162 (to I.K.); Allan Smidt Charitable Fund (to I.K.); Ralph Block Family Foundation (to I.K.); Kleeman Fund (to I.K.); the Factor Family Foundation (to I.K.); National Institutes of Health grant R61MH135106 (to N.S.); National Institutes of Health grant R01 CA221296-01A1 (to H.A.C.); UCLA Graduate Dean's Scholar Award (to J.Z.); UCLA Electrical and Computer Engineering Department Fellowship (to J.Z.); Chan Zuckerberg Biohub Chicago AWD00000302 (to H.Y., C.D.F., J.D., and S.O.K.); and National Institutes of Health grant R01HL165002 (to H.Y., C.D.F., J.D., and S.O.K.). **Author contributions:** J.Z. and S.E. conceived the project. J.Z., X.C., M.B., K.Y., Z.L., B.H., T.-Y.W., K.A.S., C.L., H.A.C., B.M.W., N.S., S.O.K., C.M., I.K., and S.E. developed the methodology. J.Z., X.C., M.B., K.Y., Z.L., B.H., T.-Y.W., J.C., J.T., J.F., Y.L., C.H., J.N., A.S., I.R., S.L., Y.Z., K.Z., H.Y., C.D.F., J.D., A.Z., Y. Chi, and Y. Chen developed and characterized the RNB electrodes. K.A.S., J.C., J.F., and R.C. developed the PCB components. J.Z. and M.B. conducted simulation studies. J.Z., T.-Y.W., J.T., C.H., I.R., D.J., L.V., and A.A. performed cell and animal studies. J.Z., X.C., M.B., and S.E. conducted visualization. J.Z., H.A.C., B.M.W., N.S., S.O.K., C.M., I.K., and S.E. acquired funding. Project administration was led by S.E. Supervision was provided by C.L., H.A.C., B.M.W., N.S., S.O.K., C.M., I.K., and S.E. J.Z., X.C., and S.E. wrote the original draft. All authors—J.Z., X.C., M.B., K.Y., Z.L., B.H., T.-Y.W., K.A.S., J.C., J.T., J.F., Y.L., C.H., J.N., A.S., I.R., S.L., Y.Z., K.Z., R.C., H.Y., C.D.F., J.D., D.J., L.V., A.A., A.Z., Y. Chi,

Y. Chen, C.L., H.A.C., B.M.W., N.S., S.O.K., C.M., I.K., and S.E.—reviewed and edited the manuscript. **Competing interests:** J.Z. and S.E. are inventors on a provisional patent application (US Prov. App. no. 63/726,149, Minimally invasive resilient nanostructured biosensing electrode directly monitors renal/hepatic drug clearance) related to some aspects of the presented technology. S.O.K. is a cofounder of cTRL Therapeutics, Arma Biosciences, and Glimmer Therapeutics. The other authors declare that they have no competing interests. **Data, code, and materials availability:** All data associated with this study are present in the paper or the Supplementary Materials. All code related to the study are available at 10.5281/zenodo.18701171. All materials used or generated in this study are commercially available or will be supplied upon reasonable request.

Submitted 13 March 2025
Resubmitted 30 July 2025
Accepted 12 March 2026
Published 1 April 2026
10.1126/scitranslmed.adr5493

Science Translational Medicine

Resilient nanostructured bioanalytic microneedle longitudinally monitors preclinical renal and hepatic drug clearance and dysfunction

Jialun Zhu, Xuanbing Cheng, Mohammadreza Bahramian, Kuanming Yao, Zongqi Li, Bintao Hu, Tsung-Yu Wu, Kiarash A. Sabet, Jiarui Cui, Jiawei Tan, Junjie Fang, Yifu Li, Connie Ho, Joshua Ng, Anthony Sung, Isabel Romero, Shuyu Lin, Yichao Zhao, Kaiji Zhang, Ryan Chaiyakul, Hanie Yousefi, Connor D. Flynn, Jagotamoy Das, David Jelinek, Laurent Voisin, Aaron Ambrus, Ao Zhang, Yitian Chi, Yu Chen, Chong Liu, Hilary A. Coller, Benjamin M. Wu, Nanthia Suthana, Shana O. Kelley, Carlos Milla, Ira Kurtz, and Sam Emaminejad

Sci. Transl. Med. **18** (843), eadr5493. DOI: 10.1126/scitranslmed.adr5493

Editor's summary

Wearable biosensors show promise for real-time in-tissue monitoring of drug pharmacokinetics, yet further advances are needed in sensitivity and mechanical resilience. Here, Zhu *et al.* present a resilient nanostructured bioelectrode (RNB) microneedle with high-sensitivity aptamer-based analyte detection from interstitial fluid. Fabricated by stress-mitigated dealloying, the strong nanostructured gold bioelectrode surface maintained better sensor response after tissue insertion compared with a nanodendrite bioelectrode. In preclinical models, the RNB detected drug clearance differences in interstitial fluid across hepatic and renal disease states, consistent with blood-based measures of drug clearance and organ function. The study demonstrates preclinical promise for minimally invasive therapeutic drug monitoring and functional assessment of hepatic and renal drug processing. —Molly Ogle

Science Translational Medicine (ISSN 1946-6242) is published by the American Association for the Advancement of Science. 1200 New York Avenue NW, Washington, DC 20005. The title *Science Translational Medicine* is a registered trademark of AAAS.